Efficient matter-wave lensing of ultracold atomic mixtures

IOP Publishing Quantum Sci. Technol. 8 (2023) 024001 https://doi.org/10.1088/2058-9565/acb16e

Quantum Science and Technology

OPEN ACCESS

RECEIVED
9 September 2022

REVISED
18 December 2022

ACCEPTED FOR PUBLICATION
9 January 2023

PUBLISHED
25 January 2023

PAPER

Efficient matter-wave lensing of ultracold atomic mixtures

Matthias Meister* and **Albert Roura**

German Aerospace Center (DLR), Institute of Quantum Technologies, Wilhelm-Runge-Straße 10, 89081 Ulm, Germany
* Author to whom any correspondence should be addressed.

E-mail: matthias.meister@dlr.de

Keywords: quantum gas mixtures, Bose–Einstein condensates, Bose–Bose mixtures, matter-wave lensing, cold atoms, tests of universality of free fall

Abstract

Mixtures of ultracold quantum gases are at the heart of high-precision quantum tests of the weak equivalence principle, where extremely low expansion rates have to be reached with matter-wave lensing techniques. We propose to simplify this challenging atom-source preparation by employing magic laser wavelengths for the optical lensing potentials, which guarantee that all atomic species follow identical trajectories and experience common expansion dynamics. In this way, the relative shape of the mixture is conserved during the entire evolution while cutting in half the number of required lensing pulses compared to standard approaches.

1. Introduction

Mixtures of ultracold quantum gases are unique systems to study a plethora of phenomena including molecule formation [1, 2] and many-body physics [3] with different isotopes and elements, the realization of shell-shaped quantum gases [4] based on interspecies repulsion [5, 6], as well as testing the universality of free fall (UFF) [7–9], where the gravitational acceleration of two different atomic species is compared by means of atom interferometric techniques [10]. Nowadays different types of atomic mixtures are studied ranging from laser-cooled thermal clouds [11, 12], Bose–Einstein condensates (BECs) [13–15], and degenerate Fermi gases [16–18] to combinations of ultracold bosons and fermions [19–21]. Despite their obvious differences, all these systems share similar experimental challenges due to the nature of a quantum gas mixture.

For instance, on Earth the gravitational sag typically leads to asymmetric states [13, 22, 23] due to different central trajectories of the individual species, as shown in the first column of figure 1 for the particular case of a ^{41}K-^{87}Rb BEC mixture. This differential sag limits the efficiency of sympathetic cooling as well as the precision of UFF tests [24–26] and prevents the formation of shell-structures for mixtures on ground [5].

A possible way of circumventing unwanted effects due to gravitational sag is the operation on microgravity platforms such as drop towers [27, 28], Einstein elevators [29], zero-g planes [30] or in space [25, 26, 31–33]. However, even then the free expansion rates of the different species do not match for the trap configurations being considered in standard setups; see middle column of figure 1. As a consequence, the relative density distributions of the mixture are deformed by the expansion dynamics, spoiling symmetric shell structures and degrading the accuracy of interferometric measurements due to relative wave-front distortions.

There are methods to engineer the expansion rates of the mixture by switching on for a short time, and after the clouds have expanded, a trapping potential that acts as a matter-wave lens. This delta-kick collimation technique [27, 28, 34–40] reduces the kinetic energy of the system and enables very low expansion rates, which are mandatory for high-precision interferometry in microgravity. However, in order to control the expansion rates of a mixture in all spatial dimensions, one lens per independent direction is required for each species, rendering a full 3D implementation rather impractical and error prone.

In this article we propose to overcome these challenges by taking advantage of optical dipole traps employing special *magic* wavelengths such that the ratio of the optical potentials for two different species j

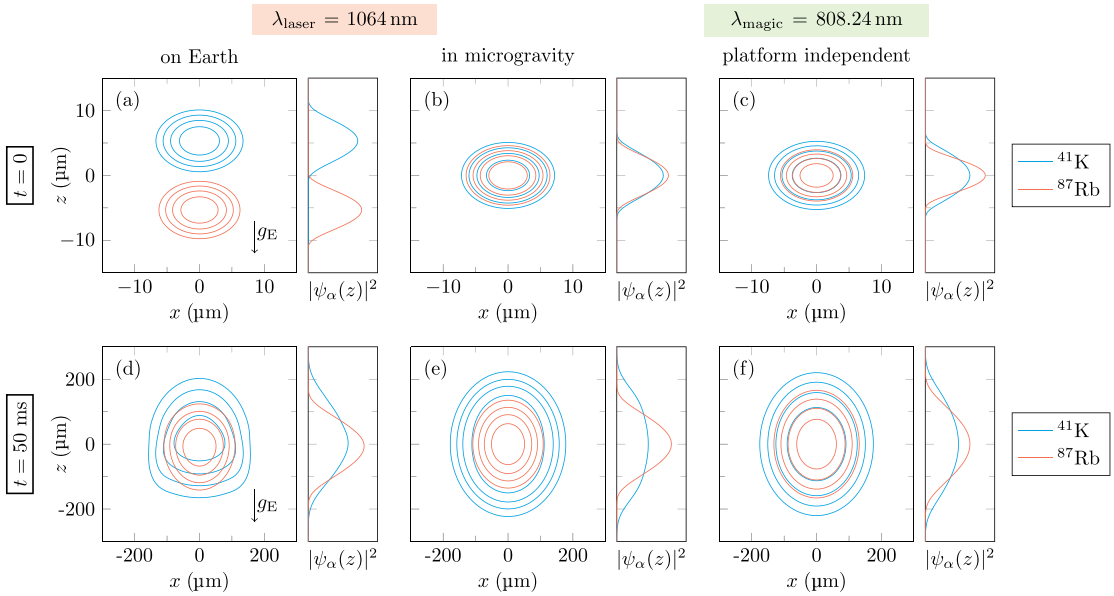

Figure 1. Integrated 2D density distributions in the comoving x-z-plane of an interacting ^{41}K-^{87}Rb BEC mixture displaying the ground state (a)–(c) and the state after 50 ms of free expansion (d)–(f) for three combinations of laser wavelengths and gravitational environments. The side panels depict the integrated 1D density along z. On Earth and in the standard case of a non-magic wavelength $\lambda_{\text{laser}} = 1064\,\text{nm}$ the gravitational acceleration $g_E = 9.81\,\text{ms}^{-2}$ leads to a relative displacement between the two condensates, potentially preventing any overlap for the ground state (a) and resulting in asymmetric and deformed densities after some time of flight (d). In microgravity the ground state is symmetric (b) but its relative shape changes after release from the trap (e) as a consequence of the different trap frequencies for both species ($\omega_{\text{Rb}} = 0.733\,\omega_{\text{K}}$). In contrast, for the magic wavelength $\lambda_{\text{magic}} = 808.24\,\text{nm}$, which yields $\omega_{\text{K}} = \omega_{\text{Rb}}$, the ground state is symmetric (c) and in addition fully conserves its relative shape during free expansion (f). The parameters for these exact numerical simulations are the trap frequency $\omega_{\text{K}} = 2\pi \cdot 100\,\text{Hz}$, the number of particles $N_{\text{K}} = N_{\text{Rb}} = 10^5$, and the s-wave scattering lengths $a_{\text{KK}} = 60a_0$, $a_{\text{RbRb}} = 100a_0$, and $a_{\text{KRb}} = 20a_0$.

and k is given by the ratio of their masses: $V_j/V_k = m_j/m_k$[1]. In this case, the classical equations of motion for the center-of-mass dynamics are identical for all species, which results in a vanishing differential gravitational sag [6, 42] and perfect co-location of the species involved even in an Earth-based laboratory; see figure 1(c).

Most importantly, as we will show here, optical dipole traps with such a magic laser wavelength guarantee that the relative shape of the mixture is conserved during the entire dynamics even for time-dependent potentials; see last column of figure 1. This property has far-reaching consequences and enables an efficient collimation of mixtures of ultracold atoms, so that very low expansion rates can be reached with fewer lensing pulses than standard approaches.

Hence, employing the magic wavelengths proposed here will drastically improve the control over the dynamics of mixture experiments, allowing new applications in ground-based setups, but also boosting long-time dual-species interferometry in space by simplifying the source preparation and at the same time minimizing spurious phase shifts due to wave-front distortions that would otherwise undermine the accuracy of the measurements.

As discussed in appendices A and B the proposed method applies to several types of mixtures, namely BECs, cold thermal clouds, and non-interacting ultracold Fermi gases, but not to Bose-Fermi mixtures. As a specific example, we will focus here on the particularly interesting case of a multi-species BEC.

2. Common dynamics for quantum gas mixtures

As long as the trapping potentials of the different atomic species fulfill the condition $V_j/V_k = m_j/m_k$, which can be achieved by employing a magic laser wavelength and also holds for gravitational and inertial forces, the classical equations of motion for the center-of-mass are identical for all species and we can describe the mixture with a comoving coordinate system that follows the classical trajectory as shown in appendix A. In this comoving frame and for locally harmonic potentials V_j (i.e. well approximated by a harmonic potential

[1] Note that for different internal states of the same atomic isotope the masses m_j and m_k are identical and one recovers the usual notion of 'magic wavelength' employed in optical atomic clocks [41].

over the size of the atomic cloud [2]), the expansion dynamics is therefore governed by potentials of the form

$$\frac{\mathcal{V}_j(\boldsymbol{x},t)}{m_j} = \frac{1}{2}\boldsymbol{x}^{\mathrm{T}}\Omega^2(t)\,\boldsymbol{x} \tag{1}$$

where m_j is the atomic mass of species j and $\Omega^2(t)$ is a 3×3 matrix containing the trap frequencies.

Since the local trap frequencies of potentials given by equation (1) are equal for all species, we can describe the time evolution of the mixture with a common scaling that conserves the relative shape of the density distributions analogously to the single-species case [43–45]. Indeed, starting with the well-known nonlinear Gross–Pitaevskii equation (GPE), the transformation

$$\psi_j(\boldsymbol{x},t) = \frac{\mathrm{e}^{\mathrm{i}\,\Phi_j(\boldsymbol{\xi},t)}}{\sqrt{\det\Lambda}}\,\psi_{\Lambda,j}(\boldsymbol{\xi},t) \tag{2}$$

of the wave function to the adapted coordinates $\boldsymbol{\xi} = \Lambda^{-1}(t)\,\boldsymbol{x}$ with the quadratic phase $\Phi_j(\boldsymbol{\xi},t)$ leads to a transformed GPE with nearly vanishing time evolution for the wave function $\psi_{\Lambda,j}(\boldsymbol{\xi},t)$ as discussed in appendix A.

The reason for this nearly frozen dynamics in the adapted coordinates is the fact that the position-dependent quadratic phase $\Phi_j(\boldsymbol{\xi},t)$ already contains the entire dynamics as long as the time-dependent Thomas–Fermi approximation is valid and locally harmonic potentials are considered. In this case, the relative shape of the wave function does not change and the time evolution in the comoving frame is fully determined by the transformation in equation (2) and the scaling matrix $\Lambda = \Lambda(t)$, which is a time-dependent 3×3 matrix that fulfills the differential equation

$$\frac{\mathrm{d}^2\Lambda}{\mathrm{d}t^2} + \Omega^2(t)\,\Lambda = \frac{\left(\Lambda^{-1}\right)^{\mathrm{T}}\Omega^2(0)}{\det\Lambda} \tag{3}$$

with the initial conditions $\Lambda(0) = \mathbb{1}$ and $\dot{\Lambda}(0) = 0$.

We emphasize that for potentials satisfying equation (1) a constant, non-vanishing interspecies interaction does not change the relative shape of the mixture during the dynamics because the effect of the interaction has already been taken into account for the initial ground state of the mixture, which is simply rescaled by the expansion dynamics as shown in the right column of figure 1.

3. Efficient atomic lensing for mixtures

Since our method works for time-dependent potentials which are locally harmonic, it can also be exploited for matter-wave lensing of the ultracold atomic mixture with delta-kick collimation techniques [27, 28, 34–40]. In general, achieving 3D collimation requires one lensing pulse for each independent direction, which for a single quantum gas in a cylindrically symmetric trap implies two pulses and four for a dual-species mixture.

By employing magic wavelengths for crossed optical dipole traps, which lead to local potentials given by equation (1) with a diagonal matrix $\Omega^2(t) = \omega^2(t)\,\mathrm{diag}(1,1,2)$, the required number of pulses for a dual-species mixture can be reduced to just two because the relative shape of the mixture is conserved by the time evolution and both species respond equally to the lensing potential.

As an especially relevant example, in figure 2 we compare the performance of a double-lens sequence acting on a ^{41}K-^{87}Rb BEC mixture for the cases of standard and magic laser wavelengths, where the results are obtained by numerically solving the GPE. During the free expansion of the mixture a first lensing pulse is applied 35 ms after release from the trap, followed by a second lensing pulse at $t = 600$ ms such that very low expansion rates are achieved for ^{41}K in all spatial directions. In addition, by means of a Feshbach resonance [46] the interspecies scattering length is tuned to the constant value $a_{\mathrm{KRb}} = 20a_0$, where a_0 is the Bohr radius, which results in a large spatial overlap of the ground state densities of the two species. All chosen parameters are realistic for operation in microgravity and in line with the requirements of future space missions for precision measurements [26].

As shown in figure 2(b), for the magic laser wavelength an almost perfect collimation can be achieved and the size of the clouds along all three spatial directions remain below 400 μm for an expansion time of

[2] In Earth-based experiments the combination of finite Gaussian beam size and gravitational sag may lead to non-negligible local anharmonicities, but they can be suppressed by employing larger beam waists and higher laser power.

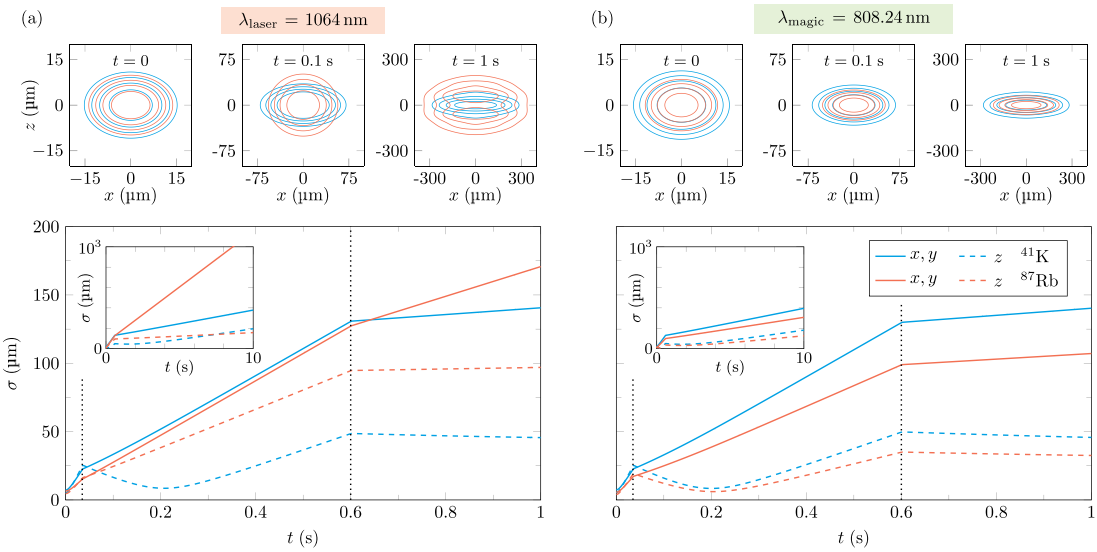

Figure 2. Time evolution of the density distributions (top) and standard deviations $\sigma(t)$ (bottom) of an interacting ^{41}K-^{87}Rb BEC mixture for a sequence of two atomic-lensing pulses. During free expansion the trapping potential is switched on again for a first (second) lens pulse 35 (600) ms after release from the trap for a duration of 1.85 (2.40) ms with frequencies scaled by a factor of 1 (1/4). For the standard laser wavelength $\lambda_{\text{laser}} = 1064$ nm (a) the lenses act differently on both species ($\omega_{\text{Rb}} = 0.733\,\omega_{\text{K}}$) resulting in an almost uncollimated expansion of the rubidium cloud (red) along the x- and y-axis and deforming the whole mixture due to interspecies interactions. On the other hand, for the magic wavelength $\lambda_{\text{magic}} = 808.24$ nm (b) simultaneous collimation for both species in all directions is naturally accomplished ($\omega_{\text{Rb}} = \omega_{\text{K}}$), the relative shape of the mixture is conserved during the entire evolution and cloud sizes below 400 μm for up to 10 s are attained (see inset), which corresponds to 3D expansion energies of 3.4 and 4.3 pK. The cylindrically symmetric setup for this numerical simulation is defined by the radial trap frequency $\omega_{\text{K}} = 2\pi \cdot 15$ Hz, the number of particles $N_{\text{K}} = N_{\text{Rb}} = 10^5$, and the s-wave scattering lengths $a_{\text{KK}} = 60a_0$, $a_{\text{RbRb}} = 100a_0$, and $a_{\text{KRb}} = 20a_0$.

10 s, which corresponds to theoretically achievable 3D expansion energies of 3.4 and 4.3 pK for ^{41}K and ^{87}Rb, respectively. Moreover, when employing a magic laser wavelength the relative shape is fully conserved during the entire evolution and irrespective of the constant interspecies scattering length.

In contrast, in the case of a standard laser wavelength, displayed in figure 2(a), the initially inner species (^{87}Rb) expands much faster after the lensing pulses (see inset for long times), which leads to strong deformations of the density distribution of both species that are enhanced by the interspecies interaction. Such behavior can lead to spurious interferometric phases that can severely compromise the measurement accuracy. Furthermore, since good collimation in all directions is only achieved for ^{41}K, the rather large expansion rate along x and y for ^{87}Rb would ultimately limit the time that the atom cloud can be potentially observed. The relatively slow expansion of ^{87}Rb in the z-direction is due to a fortunate coincidence because the frequency in this direction is very close to the one of ^{41}K in x and y, which is due to the mass ratio and polarizability of the two species.

In summary, the common translation and expansion dynamics for mixtures of ultracold atoms afforded by magic laser wavelengths is a very natural way of improving the efficiency of atomic lensing protocols, which are essential ingredients for precision UFF tests. Moreover, other applications such as studying the dynamics of quantum bubbles based on mixtures [5, 6] will particularly benefit from this approach since it enables the preparation of slowly expanding mixtures that freely evolve for a long time while preserving the shell structure. In this respect the lensing of shell mixtures is complementary to the lensing of rf-dressed shells [47].

4. Magic laser wavelengths

For the typical example of a crossed optical dipole trap [48] discussed above, the square of the radial trap frequency is given by

$$\omega_j^2 = \frac{4\,P_{\text{L}}\,\text{Re}\left[\alpha_{j,\text{L}}\right]}{\pi\,c\,\epsilon_0\,w_{\text{L}}^4\,m_j} \tag{4}$$

where P_{L} is the laser power, w_{L} the beam waist and $\alpha_{j,\text{L}}$ the polarizability, which includes the contributions from all relevant atomic transitions.

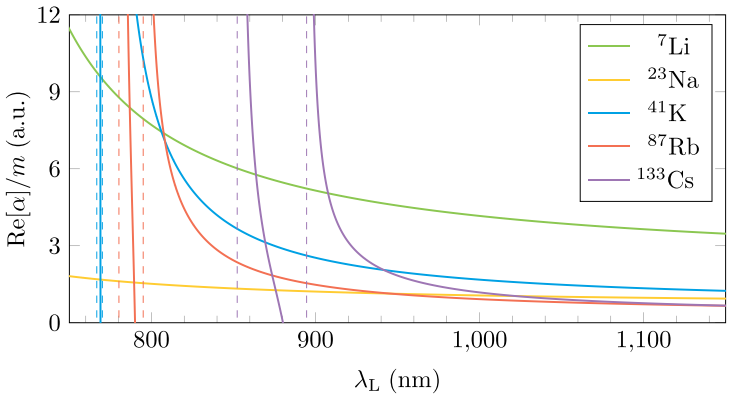

Figure 3. Polarizability α divided by the atomic mass m as a function of the laser wavelength λ_L for all stable alkaline elements. Line crossings indicate magic laser wavelengths yielding a common dynamics for the two species involved. The resonant D1- and D2-transition lines are marked by vertical dashed lines with the same color code as the polarizabilities.

From equation (4) we see that the ratio between the polarizability and the mass contains the entire species dependence of the trap frequency. In figure 3 this ratio is plotted as a function of the laser wavelength λ_L for all alkali metals. Similar calculations for the polarizability have been done before in references [49, 50]. As clearly seen in figure 3, there are several crossing points for different pairs of elements, which correspond to magic wavelengths leading to the common dynamics for both species as discussed in the present paper. The precise values of the magic wavelengths and the corresponding scattering rates for different isotope combinations can be found in appendix C.

In particular, binary combinations of ^{23}Na, ^{87}Rb, and ^{133}Cs feature crossing points far away from their transition frequencies and are therefore excellent candidates for implementing our proposed scheme. Of special interest is also the crossing of ^{41}K and ^{87}Rb at $\lambda_L = 808.24$ nm because this mixture is considered a prime candidate for future space-based tests of UFF [26]. In fact, a similar wavelength has been used in reference [42] to avoid the differential gravitational sag of a ^{40}K-^{87}Rb mixture. However, for such a Bose–Fermi mixture there is no common expansion dynamics.

5. Discussion

In order to assess the practical feasibility of magic laser wavelengths, the required laser power and atom losses due to spontaneous emission need to be considered. For the particular lensing sequence of a ^{41}K-^{87}Rb BEC mixture with the magic laser wavelength $\lambda_L = 808.24$ nm discussed in this paper (see figure 2 (b)) a beam waist of 100 (600) μm and a laser power of 2.61 (212) mW are required for the first (second) lens pulse, respectively. These parameters constitute a reduction by a factor of 5 in laser power compared with a setup based on the standard laser wavelength $\lambda_L = 1064$ nm. Hence, for currently planned high-precision UFF tests in space our approach can substantially relax the requirements on the needed laser power in addition to making the lensing process much more efficient as discussed above. The required laser light can be generated with standard diode lasers at 808 nm, which are already available for ground operations and can be further qualified for space missions. Moreover, atom losses due to off-resonant photon scattering are negligible during the rather short lensing pulses, where peak scattering rates of $7.77(17.5) \times 10^{-3}$ 1/s for ^{41}K and $35.0(78.7) \times 10^{-3}$ 1/s for ^{87}Rb for the first (second) lens occur for $\lambda_L = 808.24$ nm. For these scattering rates, performing the final evaporation in the optical trap seems feasible as well.

When comparing our approach to another recent proposal for atomic lensing of BEC mixtures [38], we identify three key improvements that result from using a magic wavelength: (a) the common dynamics enabled by the magic laser wavelength allows a reduction of the required number of lens pulses by up to a factor of 2, (b) less laser power is needed due to working with a smaller detuning, and (c) the interspecies interaction does not need to be switched to zero during the lens sequence in order to avoid deformations of the clouds, so that the scattering length can instead remain constant with a non-vanishing value during the whole process. For the ^{41}K-^{87}Rb mixture discussed in detail above, adjusting the interspecies interaction through a Feshbach resonance [46] is nevertheless required in order to obtain a miscible initial state. The large magnetic field that is applied to address the Feshbach resonance needs to be switched off after the entire lens sequence since it would disturb the interferometric measurement. By optimizing the timings of the sequence, the impact of this late change of the interspecies interaction on the expansion dynamics can be made negligible. Alternatively, by considering mixtures with a naturally low interspecies scattering length

and a miscible ground state, such as ^{84}Sr-^{86}Sr [51] or ^{87}Rb-^{168}Yb/^{170}Yb [52], there would be no need for a Feshbach field at all. In the case of rubidium and ytterbium there is no single magic wavelength, however, and thus a bichromatic optical trap is required to achieve identical trap frequencies.

Besides these crucial advantages for matter-wave lensing of ultracold atomic mixtures, there are also other applications that will benefit from magic optical wavelengths such as the generation in ground-based laboratories of shell-shaped BEC mixtures, which can be exploited to investigate curved 2D-geometries in 3D space, or the study of molecule formation on ground due to an improved overlap of the two different species involved. Lastly, our study of magic wavelengths (figure 3) has also revealed the possibility of a three-species mixture of ^{7}Li, ^{41}K, and ^{87}Rb with large spatial overlap in Earth-bound experiments that could open up new avenues in many-body physics.

Data availability statement

The data that support the findings of this study are available upon reasonable request from the authors.

Acknowledgment

The authors thank Ernst Rasel and Dennis Schlippert for insightful discussions.

Appendix A. Evolution of BEC mixtures in optical potentials for magic laser wavelengths

In this appendix we show that in the case of magic laser wavelengths and for locally harmonic potentials the central trajectories of all atomic species are identical for quantum gas mixtures and that the evolution of the centered wave packets can be described by a single scaling in the case of BEC mixtures.

A.1. Classical equations of motion

From the classical equation of motion $m\ddot{\boldsymbol{x}} = -\boldsymbol{\nabla} V$ it is clear that when the ratio V_j/m_j is the same for different atomic species (labeled here with the subindex j), both the equations and the corresponding solutions will be the same for all species. Furthermore, given any external potentials with this property, such as the optical potentials for magic laser wavelengths considered in this article, the same conclusions will also apply in the presence of a gravitational field, as can be immediately seen from the equation of motion in that case:

$$m_j\ddot{\boldsymbol{x}} = -\boldsymbol{\nabla}\left(V_j(\boldsymbol{x},t) + m_j U(\boldsymbol{x},t)\right), \tag{A.1}$$

where $U(\boldsymbol{x},t)$ is the gravitational potential. In addition, the result can be straightforwardly generalized to include the effects of inertial forces as well (for example, due to accelerations and rotations of the experimental setup) and it leads in all cases to identical trajectories for the different atomic species.

In particular, this implies that the gravitational sag for a trap potential, which can be determined by taking $\ddot{\boldsymbol{x}} = 0$ on the left-hand side of equation (A.1), will be the same for all species. Moreover, the frequency matrix $(\Omega^2)_{ab} = (1/m_j)\,\partial^2 V_j/\partial x_a \partial x_b$ at the trap minimum will be common for all atomic species and, more generally, this will also hold for the local frequency matrix obtained by evaluating the second derivatives of the potential at any other position. As a simple example, if we consider a harmonic external potential in a uniform gravitational field, corresponding to $U(\boldsymbol{x}) = U_0 - \boldsymbol{g}\cdot\boldsymbol{x}$, and with one of its principal axis aligned with the gravitational acceleration $\boldsymbol{g}$, the resulting gravitational sag is $\Delta z = -g/\omega_z^2$. Here ω_z^2 is the eigenvalue of the matrix Ω^2, which in this case is spatially independent, along the direction of the gravitational field. For non-uniform gravitational fields gravity gradients lead to non-vanishing second derivatives of the gravitational potential U, whose contribution can be included in the frequency matrix Ω^2. In practice, however, such contributions are much smaller than those from the external potential V_j and can typically be neglected.

A.2. Propagation of matter wave packets

Interestingly, the above conclusions for the classical case can be naturally extended to the quantum dynamics of matter wave packets and atomic clouds. In order to show this point, it is particularly useful to consider a description of matter wave propagation in terms of *central trajectories* and *centered wave packets* [24, 45, 53, 54] which is applicable to a very broad range of situations, including a relativistic description of matter wave propagation in curved spacetime [55]. Further details can be found in the quoted references, but the key result is that the wave-packet evolution can be expressed as follows:

$$\psi_j(\boldsymbol{x},t) = \mathrm{e}^{\mathrm{i}S_j/\hbar}\,\mathrm{e}^{\mathrm{i}\boldsymbol{P}(t)\cdot(\boldsymbol{x}-\boldsymbol{X}(t))/\hbar}\,\psi_j^{(c)}\left(\boldsymbol{x}-\boldsymbol{X}(t),t\right), \tag{A.2}$$

where $\boldsymbol{X}(t)$ and $\boldsymbol{P}(t) = m_j\dot{\boldsymbol{X}}(t)$ correspond to the central trajectory and satisfy the classical equations of motion, $\psi_j^{(c)}$ is the centered wave function, and the phase S_j is given by the classical action

$$S_j = \int_{t_0}^{t} \mathrm{d}t' \left(\frac{1}{2} m_j \dot{\boldsymbol{X}}^2 - V_j(\boldsymbol{X}, t') - m_j U(\boldsymbol{X}, t') \right). \tag{A.3}$$

More importantly for our considerations in the present paper, the evolution of the centered wave packet is governed by the following Schrödinger equation:

$$\mathrm{i}\hbar \frac{\partial}{\partial t} \psi_j^{(c)}(\boldsymbol{x}', t) = \left[-\frac{\hbar^2}{2m_j} \nabla_{\boldsymbol{x}'}^2 + \mathcal{V}_j(\boldsymbol{x}', t) \right] \psi_j^{(c)}(\boldsymbol{x}', t), \tag{A.4}$$

where we have introduced the comoving coordinate $\boldsymbol{x}' = \boldsymbol{x} - \boldsymbol{X}$ and $\mathcal{V}_j(\boldsymbol{x}', t) \equiv V_j(\boldsymbol{X} + \boldsymbol{x}', t) - V_j(\boldsymbol{X}, t) - \boldsymbol{x}' \cdot \boldsymbol{\nabla} V_j(\boldsymbol{X}, t)$, which reduces to the purely quadratic part when V_j is a harmonic potential. For non-uniform fields the gravitational potential U gives rise to a contribution analogous to $\mathcal{V}_j$, but it is typically much smaller and has been omitted here. Note also that in the main text, e.g. in equations (1) and (2) and figures 1 and 2, we have used $\boldsymbol{x}$ instead of $\boldsymbol{x}'$ for the comoving coordinates in order to ease the notation.

For BECs and BEC mixtures, one needs to add the mean-field interaction term and obtains then the GPE for the centered wave functions describing the multispecies condensate in the mean-field approximation:

$$\mathrm{i}\hbar \frac{\partial}{\partial t} \psi_j^{(c)}(\boldsymbol{x}', t) = \left[-\frac{\hbar^2}{2m_j} \nabla_{\boldsymbol{x}'}^2 + \mathcal{V}_j(\boldsymbol{x}', t) + \sum_k g_{jk} \left| \psi_k^{(c)}(\boldsymbol{x}', t) \right|^2 \right] \psi_j^{(c)}(\boldsymbol{x}', t), \tag{A.5}$$

where the subindex j labels the atomic species and we have taken into account that for the potentials being considered the central trajectory $\boldsymbol{X}(t)$ is the same for all species. If in addition the potential can be regarded as locally harmonic (i.e. well approximated by a harmonic potential over the size of the atomic cloud), in equation (A.5) one can simply take

$$\mathcal{V}_j(\boldsymbol{x}', t) = \frac{m_j}{2} \boldsymbol{x}'^{\mathrm{T}} \Omega^2(t) \boldsymbol{x}', \tag{A.6}$$

with a common frequency matrix $\Omega^2(t)$ for all species and corresponding to the second derivatives of the potential evaluated at the central trajectory: $(\Omega^2)_{ab}(t) = (1/m_j)\, \partial^2 V_j / \partial x_a \partial x_b \big|_{\boldsymbol{x}=\boldsymbol{X}(t)}$.

The initial ground state of the mixture is in this case determined by the time-independent GPE

$$\mu_j' \psi_j^{(c)}(\boldsymbol{x}', 0) = \left[\frac{m_j}{2} \boldsymbol{x}'^{\mathrm{T}} \Omega^2(0) \boldsymbol{x}' + \sum_k g_{jk} \left| \psi_k^{(c)}(\boldsymbol{x}', 0) \right|^2 \right] \psi_j^{(c)}(\boldsymbol{x}', 0) \tag{A.7}$$

where μ_j' is the chemical potential of species j. The chemical potential μ_j' is defined here with respect to the potential $\mathcal{V}_j$. Strictly speaking, in general one may need to add $\boldsymbol{x}'$-independent terms analogous to those in equation (A.3), which can be important when the condensate mixture interacts with an external particle reservoir, but are not relevant for our considerations.

A.3. Scaling approach and time-dependent Thomas–Fermi approximation

In the case of identical central trajectories and locally harmonic potentials described above, the (quantum) dynamics of the centered wave packets, which includes the size evolution of the BEC mixture, can be determined quite efficiently without having to solve the coupled system of nonlinear partial differential equation (A.5) explicitly. In fact, for potentials given by equation (A.6) the relative shape of the initial density distribution of the mixture is conserved during the time evolution, so that for constant interaction strengths the time-dependent wave functions are governed by a single scaling law analogous to the scaling solution for single-species BECs [43–45].

To prove this statement, we introduce the rescaled coordinates

$$\boldsymbol{\xi} = \Lambda^{-1}(t) \boldsymbol{x}', \tag{A.8}$$

with the time-dependent 3×3 scaling matrix $\Lambda(t)$, and perform a transformation of the centered wave functions

$$\psi_j^{(c)}(\boldsymbol{x}', t) = \frac{\mathrm{e}^{\mathrm{i}\Phi_j(\boldsymbol{\xi}, t)}}{\sqrt{\det \Lambda(t)}} \psi_{\Lambda, j}(\boldsymbol{\xi}, t), \tag{A.9}$$

with

$$\Phi_j(\boldsymbol{\xi},t) = -\frac{\beta_j(t)}{\hbar} + \frac{m_j}{2\hbar}(\Lambda\boldsymbol{\xi})^{\mathrm{T}}\frac{\mathrm{d}\Lambda}{\mathrm{d}t}\boldsymbol{\xi}, \tag{A.10}$$

and

$$\beta_j(t) = \int_{t_0}^{t} \mathrm{d}t' \frac{\mu_j'}{\det\Lambda(t')}. \tag{A.11}$$

By applying this transformation to equation (A.5) and arranging the terms appropriately, we obtain the rescaled differential equation

$$\mathrm{i}\hbar\frac{\partial}{\partial t}\psi_{\Lambda,j}(\boldsymbol{\xi},t) = \left[H_j^{(1)}(\boldsymbol{\xi},t) + H_j^{(2)}(\boldsymbol{\xi},t)\right]\psi_{\Lambda,j}(\boldsymbol{\xi},t), \tag{A.12}$$

for the centered wave packets and with the position- and time-dependent terms

$$H_j^{(1)}(\boldsymbol{\xi},t) = -\frac{\hbar^2}{2m_j}\nabla_{\boldsymbol{\xi}}^{\mathrm{T}}\Lambda^{-1}\left(\Lambda^{-1}\right)^{\mathrm{T}}\nabla_{\boldsymbol{\xi}}, \tag{A.13}$$

and

$$H_j^{(2)}(\boldsymbol{\xi},t) = \frac{1}{\det\Lambda}\left[\frac{m_j}{2}\boldsymbol{\xi}^{\mathrm{T}}\Omega^2(0)\boldsymbol{\xi} + \sum_k g_{jk}\left|\psi_{\Lambda,k}(\boldsymbol{\xi},t)\right|^2 - \mu_j'\right]. \tag{A.14}$$

Up to this point the rescaled GPE (A.12) is exact as long as the scaling matrix $\Lambda = \Lambda(t)$ fulfills the ordinary differential equation

$$\frac{\mathrm{d}^2\Lambda}{\mathrm{d}t^2} + \Omega^2(t)\Lambda = \frac{\left(\Lambda^{-1}\right)^{\mathrm{T}}\Omega^2(0)}{\det\Lambda}, \tag{A.15}$$

with the initial conditions

$$\Lambda(0) = \mathbb{1} \qquad \text{and} \qquad \left.\frac{\mathrm{d}\Lambda}{\mathrm{d}t}\right|_{t=0} = 0\,. \tag{A.16}$$

Clearly, the above transformation requires identical central trajectories and a common frequency matrix $\Omega^2(t)$ for all species, so that a single scaling matrix $\Lambda(t)$ is sufficient to capture the evolution of the entire mixture. In the usual case of different trap frequencies for the atomic species, different scalings are necessary for the individual species, which leads to approximate solutions for the mixture dynamics as discussed in reference [38]. In particular, the miscible and immiscible regions of the mixture would expand differently for unequal trap frequencies and give rise to shape deformations, whereas in the case of a common frequency matrix the whole mixture evolves uniformly.

Indeed, as we will show in the following, there is nearly no dynamics of the centered wave packets in the rescaled coordinates and the time evolution is almost entirely determined by the transformation (A.9). First, the contribution of the kinetic term $H_j^{(1)}$, defined in equation (A.13), can be neglected based on the well-known time-dependent Thomas–Fermi approximation [15] which is valid as long as the density distributions only undergo spatial changes on length scales larger then the healing length. For the parameters of typical experiments discussed here this assumption is already fulfilled for the ground state of the mixture and stays valid during the time evolution since most of the dynamics is included in the quadratic phase (A.10).

Next, one can show that the remaining differential equation, governed by the term $H_j^{(2)}$ defined in equation (A.14), conserves the density $|\psi_{\Lambda,j}(\boldsymbol{\xi},t)|^2$ over time because $H_j^{(2)}$ is real and acts only on position space. Thus, we obtain

$$|\psi_{\Lambda,j}(\boldsymbol{\xi},t)|^2 \approx |\psi_{\Lambda,j}(\boldsymbol{\xi},0)|^2 \tag{A.17}$$

and the rescaled GPE (A.12) can be written as

$$i\hbar\frac{\partial}{\partial t}\psi_{\Lambda,j}(\boldsymbol{\xi},t) \approx \frac{1}{\det\Lambda}\left[\frac{m_j}{2}\boldsymbol{\xi}^{\mathrm{T}}\Omega^2(0)\boldsymbol{\xi} + \sum_k g_{jk}\left|\psi_{\Lambda,k}(\boldsymbol{\xi},0)\right|^2 - \mu_j'\right]\psi_{\Lambda,j}(\boldsymbol{\xi},t). \tag{A.18}$$

Since due to the initial conditions (A.16) we obtain the relation $|\psi_j^{(c)}(\boldsymbol{x}',0)|^2 = |\psi_{\Lambda,j}(\boldsymbol{\xi},0)|^2$, we can make use of the time-independent GPE (A.7) to show that the right hand side of the differential equation (A.18) vanishes:

$$\mathrm{i}\hbar\frac{\partial}{\partial t}\psi_{\Lambda,j}(\boldsymbol{\xi},t) \approx 0. \tag{A.19}$$

Hence, the dynamics in the adapted coordinates is practically frozen: $\psi_{\Lambda,j}(\boldsymbol{\xi},t) \approx \psi_{\Lambda,j}(\boldsymbol{\xi},0) \approx \psi_j^{(c)}(\boldsymbol{x}',0)$. Therefore, the dynamics in the comoving frame is given by the initial density profile $\psi_j^{(c)}(\boldsymbol{x}',0)$ and the transformation (A.9) which is governed by the time-dependent scaling matrix $\Lambda(t)$ determined by equation (A.15).

The scaling approach enables an efficient description of the dynamics of BEC mixtures since it only requires the solution of the ordinary differential equation (A.15). The resulting solutions are valid as long as the time-dependent Thomas–Fermi approximation holds, which is the case in many practical implementations and setups.

Moreover, the scaling matrix $\Lambda(t)$ and the transformation (A.9) can also be used to accelerate the exact numerical integration of the GPE. Since most of the dynamics is absorbed in the transformation (A.9) a numerical simulation based on the rescaled coordinates (A.8) can be very efficient because only the remaining dynamics of the transformed GPE (A.12) needs to be computed which is far less demanding than a simulation of the full GPE (A.5) in the lab coordinates.

The numerical results shown in this paper were obtained by solving the transformed GPE (A.12) with an embedded Runge–Kutta method. In case of different frequency matrices $\Omega^2(t)$ for the species involved, an average scaling can still be used to reduce the computational costs of the numerical simulation.

Appendix B. Quantum-degenerate Fermi gases and thermal clouds

Besides BEC mixtures there are several other cases where magic-wavelength optical potentials can lead to a common expansion dynamics.

(a) *Non-interacting fermions:* Let us consider the ground state of a quantum-degenerate gas of non-interacting identical fermions (e.g. spin-polarized atoms) in a harmonic trap with frequency matrix $\Omega^2(0)$. At time $t = 0$ the quantum gas is released from the trap or, more generally, one has a time-dependent harmonic potential with frequency matrix $\Omega^2(t)$ for $t > 0$. In this case, the expansion dynamics can also be described in terms of a time-dependent rescaling $\boldsymbol{\xi} = \Lambda_{\mathrm{F}}^{-1}(t)\boldsymbol{x}'$ provided that the principal directions of the frequency matrix remain constant in time. Indeed, in that case it can be shown [56] that the time evolution of the one-particle phase-space distribution is entirely captured by a rescaling matrix $\Lambda_{\mathrm{F}}(t)$ satisfying the following ordinary differential equation with initial conditions given by equation (A.16):

$$\frac{\mathrm{d}^2\Lambda_{\mathrm{F}}}{\mathrm{d}t^2} + \Omega^2(t)\,\Lambda_{\mathrm{F}} = \left(\Lambda_{\mathrm{F}}^{-1}\right)^{\mathrm{T}}\Omega^2(0)\,\Lambda_{\mathrm{F}}^{-1}\left(\Lambda_{\mathrm{F}}^{-1}\right)^{\mathrm{T}}, \tag{B.1}$$

and the dynamics of the scaling factor along each principal direction actually decouples from the rest. The ordinary particle density distribution can be straightforwardly obtained from the phase-space distribution by integrating over the momentum and one gets $n(\boldsymbol{x}',t) = n\big(\Lambda_{\mathrm{F}}^{-1}(t)\boldsymbol{x}',0\big)$.

For a mixture of non-interacting fermionic species the previous result will separately hold for each one of the atomic species. Hence, since the time evolution of the scaling matrix is entirely determined by the frequency matrix, magic-wavelength optical potentials will lead to a common matrix $\Lambda_{\mathrm{F}}(t)$ for all species.

(b) *Bose–Fermi mixtures:* From equations (A.15) and (B.1) we see that the scaling matrices for BECs and Fermi gases satisfy different differential equations, which lead in general to inequivalent expansion dynamics even for a common frequency matrix $\Omega^2(t)$ and vanishing interspecies interaction. It is therefore not possible to have a common expansion dynamics for Bose–Fermi mixtures even when employing a magic wavelength for the optical potential.

(c) *Thermal clouds:* In fact, one can show that the scaling associated with the matrix $\Lambda_{\mathrm{F}}(t)$ satisfying equation (B.1) can describe the expansion dynamics of any non-interacting quantum gas (either bosonic or fermionic) provided that they are initially in a stationary state of the trap potential [57] with frequency matrix $\Omega^2(0)$. Such stationary states include energy eigenstates but also mixed states such as thermal states. Therefore, magic-wavelength optical potentials will also give rise to a common expansion dynamics of the different atomic species in sufficiently dilute thermal clouds where interatomic interactions can be neglected.

Appendix C. Optical dipole potentials

C.1. General relations for optical dipole traps

Neutral atoms can be trapped by the dipole force generated with off-resonant laser fields [48]. The corresponding optical dipole potential $V_j(\boldsymbol{x},t)$ for atoms of species j is then given by

$$V_j(\boldsymbol{x},t) = -\frac{1}{2\varepsilon_0 c}\,\mathrm{Re}\left[\alpha_{j,\mathrm{L}}\right] I_\mathrm{L}(\boldsymbol{x},t)\,, \tag{C.1}$$

where $I_\mathrm{L}(\boldsymbol{x},t)$ is the laser intensity and

$$\mathrm{Re}\left[\alpha_{j,\mathrm{L}}\right] = \pi c^3 \varepsilon_0 \sum_k \frac{f_k}{\omega_k^3}\left(\frac{\Gamma_k}{\omega_k-\omega_\mathrm{L}} + \frac{\Gamma_k}{\omega_k+\omega_\mathrm{L}}\right) \tag{C.2}$$

is the real part of the polarizability, which contains contributions from all relevant atomic transition lines labeled by the index k. Here ω_L is the laser frequency, ω_k the transition frequency, Γ_k the natural line width, and $f_k = (2J_k+1)/(2J_0+1)$ the degeneracy factor with J_0 and J_k corresponding to the quantum number of the total electron angular momentum of the ground and excited state, respectively. For the D1 and D2 transition lines of alkaline elements we obtain $f_{\mathrm{D1}} = 1$ and $f_{\mathrm{D2}} = 2$. We emphasize that equation (C.2) is valid far away from the resonances, i.e. $|\omega_k - \omega_\mathrm{L}| \gg \Gamma_k$, which is fulfilled for all the laser frequencies considered in this paper. In addition, we consider linearly polarized light parallel to the quantization axis (typically determined by an external bias magnetic field) for the optical dipole lasers. This choice ensures the degeneracy of the magnetic sublevels of the ground state manifold and thus equal energy shifts [48]. For circularly polarized light this degeneracy is lifted and trapping all magnetic sublevels in a potential with equal trap frequencies would be more involved.

For the typical case of a red-detuned crossed optical dipole trap the combined intensity of the two Gaussian beams in the harmonic approximation is given by the relation

$$I_\mathrm{L}(\boldsymbol{x},t) = \frac{4P_\mathrm{L}(t)}{\pi w_\mathrm{L}^4}\left(w_\mathrm{L}^2 - x^2 - y^2 - 2z^2\right)\,, \tag{C.3}$$

where $P_\mathrm{L}(t)$ is the laser power and w_L the beam waist. The resulting optical dipole potential has the cylindrical symmetric form $V_j(\boldsymbol{x},t) = m_j\omega_j^2(x^2+y^2+2z^2)/2$ and is determined by the radial trap frequency

$$\omega_j^2 = \frac{4\,P_\mathrm{L}\,\mathrm{Re}\left[\alpha_{j,\mathrm{L}}\right]}{\pi\, c\,\epsilon_0\, w_\mathrm{L}^4\, m_j}\,. \tag{C.4}$$

Hence, equal trap frequencies and therefore common dynamics for an atomic mixture can be achieved if the ratio $\mathrm{Re}\left[\alpha_{j,\mathrm{L}}\right]/m_j$ is identical for all the species involved.

Even though the laser frequency is chosen to be far from the transition lines there are still atom losses from the optical trap due to off-resonant photon scattering. The scattering rate is given by

$$\Gamma_{j,\mathrm{L}}(\boldsymbol{x},t) = \frac{\omega_\mathrm{L}^3\,|\alpha_{j,\mathrm{L}}|^2}{6\pi\hbar c^4\varepsilon_0^2} I_\mathrm{L}(\boldsymbol{x},t)\,, \tag{C.5}$$

where for large detunings the square of the absolute value of the polarizability can be approximated by its real part $|\alpha_{j,\mathrm{L}}|^2 \approx (\mathrm{Re}\left[\alpha_{j,\mathrm{L}}\right])^2$. The peak scattering rate occurs for the maximum laser intensity at the center of the crossed optical dipole trap and can thus be written as

$$\Gamma_{\mathrm{peak},j,\mathrm{L}}(t) = \frac{2\omega_\mathrm{L}^3 P_\mathrm{L}(t)\,|\alpha_{j,\mathrm{L}}|^2}{3\pi^2\hbar c^4\varepsilon_0^2 w_\mathrm{L}^2}\,. \tag{C.6}$$

The lifetime of the atoms in the trap can be estimated by the inverse of the peak scattering rate.

C.2. Magic optical wavelengths for atomic mixtures

There is a large variety of possible isotope combinations that can benefit from using a magic wavelength to circumvent the differential gravitational sag for the mixture and to achieve a common expansion dynamics. Table C1 gives an overview of all possible binary mixtures between stable bosonic alkaline elements and their corresponding magic laser wavelength. These wavelengths were calculated based on equations (C.2) and (C.4) by taking into account the D1 and D2 transition lines for each isotope.

In order to avoid severe atom losses due to off-resonant photon scattering, only magic wavelengths red-detuned with respect to all atomic transition lines are considered and not those located between the

Table C1. Magic laser wavelengths and relative photon scattering rates for dual-species mixtures of different alkaline isotopes. The relative scattering rates are calculated in comparison to a reference case with laser wavelength $\lambda_{L_0} = 1064\,\mathrm{nm}$ and the laser power is chosen so that the trap frequencies, given by equation (C.4), are identical for the different laser wavelengths. Only magic laser wavelengths below $2\,\mu\mathrm{m}$ are considered.

isotopes j, k	$\lambda_{\mathrm{magic}}\,\mathrm{nm}^{-1}$	$\frac{\Gamma_{j,\mathrm{magic}}}{\Gamma_{j,\mathrm{L}_0}}$	$\frac{\Gamma_{k,\mathrm{magic}}}{\Gamma_{k,\mathrm{L}_0}}$
Li7, Na23	—	—	—
Li7, K39	808.92	4.4	11.0
Li7, K41	806.13	4.5	11.9
Li7, Rb87	807.48	4.4	21.8
Li7, Cs133	907.71	2.1	9.4
Na23, K39	—	—	—
Na23, K41	—	—	—
Na23, Rb87	946.00	1.6	2.1
Na23, Cs133	1022.05	1.2	1.4
K39, Rb87	806.77	11.7	22.8
K41, Rb87	808.24	11.2	20.9
K39, Cs133	937.09	2.1	3.7
K41, Cs133	941.60	2.1	3.4
Rb87, Cs133	1164.08	0.64	0.57

transition lines of one of the two species. Moreover, to better assess the feasibility for the individual combinations, the scattering rate for each species caused by the magic wavelength is compared to the scattering rate for the reference laser wavelength $\lambda_{L_0} = 1064\,\mathrm{nm}$. For certain combinations, this comparison is quite favorable, so that we expect a broad application of magic wavelengths for mixtures of ultracold atoms in the future.

For mixtures including non-alkaline elements the corresponding magic wavelengths can be calculated in the same way. However, for some particular interesting combinations of rubidium with either strontium or ytterbium there is no single magic wavelength available due to the rather different electronic structure of the atoms and therefore widely separated transition lines. This case requires bichromatic optical dipole traps, which enable the adjustment of the trap frequency ratio through the laser powers [50, 58]. For instance a combination of laser light at 532 nm and 1064 nm, which could be generated by frequency-doubling, would be suitable for a mixture of ^{87}Rb-^{168}Yb/^{170}Yb.

ORCID iDs

Matthias Meister https://orcid.org/0000-0001-7210-8588
Albert Roura https://orcid.org/0000-0002-8049-8982

References

[1] Köhler T, Góral K and Julienne P S 2006 Production of cold molecules via magnetically tunable Feshbach resonances *Rev. Mod. Phys.* **78** 1311
[2] Carr L D, DeMille D, Krems R V and Ye J 2009 Cold and ultracold molecules: science, technology and applications *New J. Phys.* **11** 055049
[3] Bloch I, Dalibard J and Zwerger W 2008 Many-body physics with ultracold gases *Rev. Mod. Phys.* **80** 885
[4] Carollo R A, Aveline D C, Rhyno B, Vishveshwara S, Lannert C, Murphree J D, Elliott E R, Williams J R, Thompson R J and Lundblad N 2022 Observation of ultracold atomic bubbles in orbital microgravity *Nature* **606** 281
[5] Wolf A, Boegel P, Meister M, Balaž A, Gaaloul N and Efremov M A 2022 Shell-shaped Bose-Einstein condensates based on dual-species mixtures *Phys. Rev.* A **106** 013309
[6] Jia F, Huang Z, Qiu L, Zhou R, Yan Y and Wang D 2022 Expansion dynamics of a shell-shaped Bose-Einstein condensate *Phys. Rev. Lett.* **129** 243402
[7] Schlippert D, Hartwig J, Albers H, Richardson L L, Schubert C, Roura A, Schleich W P, Ertmer W and Rasel E M 2014 Quantum test of the universality of free fall *Phys. Rev. Lett.* **112** 203002
[8] Rosi G, D'Amico G, Cacciapuoti L, Sorrentino F, Prevedelli M, Zych M, Brukner Č and Tino G M 2017 Quantum test of the equivalence principle for atoms in coherent superposition of internal energy states *Nat. Commun.* **8** 15529
[9] Asenbaum P, Overstreet C, Kim M, Curti J and Kasevich M A 2020 Atom-interferometric test of the equivalence principle at the 10^{-12} level *Phys. Rev. Lett.* **125** 191101
[10] Cronin A D, Schmiedmayer J and Pritchard D E 2009 Optics and interferometry with atoms and molecules *Rev. Mod. Phys.* **81** 1051
[11] Metcalf H and van der Straten P 1994 Cooling and trapping of neutral atoms *Phys. Rep.* **244** 203
[12] Phillips W D 1998 Nobel lecture: laser cooling and trapping of neutral atoms *Rev. Mod. Phys.* **70** 721
[13] Modugno G, Modugno M, Riboli F, Roati G and Inguscio M 2002 Two atomic species superfluid *Phys. Rev. Lett.* **89** 190404
[14] Papp S B, Pino J M and Wieman C E 2008 Tunable miscibility in a dual-species Bose-Einstein condensate *Phys. Rev. Lett.* **101** 040402

[15] Dalfovo F, Giorgini S, Pitaevskii L P and Stringari S 1999 Theory of Bose-Einstein condensation in trapped gases *Rev. Mod. Phys.* **71** 463
[16] Taglieber M, Voigt A-C, Aoki T, Hänsch T W and Dieckmann K 2008 Quantum degenerate two-species Fermi-Fermi mixture coexisting with a Bose-Einstein condensate *Phys. Rev. Lett.* **100** 010401
[17] Wille E *et al* 2008 Exploring an ultracold Fermi-Fermi mixture: interspecies Feshbach resonances and scattering properties of ^{6}Li and ^{40}K *Phys. Rev. Lett.* **100** 053201
[18] Giorgini S, Pitaevskii L P and Stringari S 2008 Theory of ultracold atomic Fermi gases *Rev. Mod. Phys.* **80** 1215
[19] Hadzibabic Z, Stan C A, Dieckmann K, Gupta S, Zwierlein M W, Görlitz A and Ketterle W 2002 Two-species mixture of quantum degenerate Bose and Fermi gases *Phys. Rev. Lett.* **88** 160401
[20] Modugno G, Roati G, Riboli F, Ferlaino F, Brecha R J and Inguscio M 2002 Collapse of a degenerate Fermi gas *Science* **297** 2240
[21] Ospelkaus S, Ospelkaus C, Humbert L, Sengstock K and Bongs K 2006 Tuning of heteronuclear interactions in a degenerate Fermi-Bose mixture *Phys. Rev. Lett.* **97** 120403
[22] Myatt C J, Burt E A, Ghrist R W, Cornell E A and Wieman C E 1997 Production of two overlapping Bose-Einstein condensates by sympathetic cooling *Phys. Rev. Lett.* **78** 586
[23] Riboli F and Modugno M 2002 Topology of the ground state of two interacting Bose-Einstein condensates *Phys. Rev.* A **65** 063614
[24] Hogan J M, Johnson D M S and Kasevich M A 2008 Light-pulse atom interferometry (arXiv:0806.3261)
[25] Aguilera D N *et al* 2014 STE-QUEST–test of the universality of free fall using cold atom interferometry *Class. Quantum Grav.* **31** 115010
[26] Battelier B *et al* 2021 Exploring the foundations of the physical universe with space tests of the equivalence principle *Exp. Astron.* **51** 1695
[27] Müntinga H *et al* 2013 Interferometry with Bose-Einstein condensates in microgravity *Phys. Rev. Lett.* **110** 093602
[28] Deppner C *et al* 2021 Collective-mode enhanced matter-wave optics *Phys. Rev. Lett.* **127** 100401
[29] Condon G *et al* 2019 All-optical Bose-Einstein condensates in microgravity *Phys. Rev. Lett.* **123** 240402
[30] Barrett B, Antoni-Micollier L, Chichet L, Battelier B, Lévèque T, Landragin A and Bouyer P 2016 Dual matter-wave inertial sensors in weightlessness *Nat. Commun.* **7** 13786
[31] Becker D *et al* 2018 Space-borne Bose–Einstein condensation for precision interferometry *Nature* **562** 391
[32] Aveline D C *et al* 2020 Observation of Bose–Einstein condensates in an Earth-orbiting research lab *Nature* **582** 193
[33] Frye K *et al* 2021 The Bose-Einstein condensate and cold atom laboratory *EPJ Quantum Technol.* **8** 1
[34] Chu S, Bjorkholm J E, Ashkin A, Gordon J P and Hollberg L W 1986 Proposal for optically cooling atoms to temperatures of the order of 10^{-6} K *Opt. Lett.* **11** 73
[35] Ammann H and Christensen N 1997 Delta kick cooling: a new method for cooling atoms *Phys. Rev. Lett.* **78** 2088
[36] McDonald G D, Kuhn C C N, Bennetts S, Debs J E, Hardman K S, Johnsson M, Close J D and Robins N P 2013 80$\hbar k$ momentum separation with Bloch oscillations in an optically guided atom interferometer *Phys. Rev.* A **88** 053620
[37] Kovachy T, Hogan J M, Sugarbaker A, Dickerson S M, Donnelly C A, Overstreet C and Kasevich M A 2015 Matter wave lensing to pico kelvin temperatures *Phys. Rev. Lett.* **114** 143004
[38] Corgier R, Loriani S, Ahlers H, Posso-Trujillo K, Schubert C, Rasel E M, Charron E and Gaaloul N 2020 Interacting quantum mixtures for precision atom interferometry *New J. Phys.* **22** 123008
[39] Pandey S, Mas H, Vasilakis G and von Klitzing W 2021 Atomtronic matter-wave lensing *Phys. Rev. Lett.* **126** 170402
[40] Gaaloul N *et al* 2022 A space-based quantum gas laboratory at picokelvin energy scales *Nat. Commun.* **13** 7889
[41] Ludlow A D, Boyd M M, Ye J, Peik E and Schmidt P O 2015 Optical atomic clocks *Rev. Mod. Phys.* **87** 637
[42] Ospelkaus-Schwarzer S 2006 Quantum degenerate Fermi-Bose mixtures of ^{40}K and ^{87}Rb in 3D optical lattices *PhD Thesis* Universität Hamburg
[43] Castin Y and Dum R 1996 Bose-Einstein condensates in time dependent traps *Phys. Rev. Lett.* **77** 5315
[44] Kagan Y, Surkov E L and Shlyapnikov G V 1996 Evolution of a Bose-condensed gas under variations of the confining potential *Phys. Rev.* A **54** R1753
[45] Meister M, Arnold S, Moll D, Eckart M, Kajari E, Efremov M A, Walser R and Schleich W P 2017 Efficient description of Bose-Einstein condensates in time-dependent rotating traps *Advances In Atomic, Molecular and Optical Physics* ed E Arimondo, C C Lin and S F Yelin (London: Elsevier) vol 66 pp 375–438
[46] Thalhammer G, Barontini G, De Sarlo L, Catani J, Minardi F and Inguscio M 2008 Double species Bose-Einstein condensate with tunable interspecies interactions *Phys. Rev. Lett.* **100** 210402
[47] Boegel P, Wolf A, Meister M and Efremov M A 2022 Matter-wave lensing of shell-shaped Bose-Einstein condensates (arXiv:2209.04672)
[48] Grimm R, Weidemüller M and Ovchinnikov Y B 2000 Optical dipole traps for neutral atoms *Advances In Atomic, Molecular and Optical Physics* ed B Bederson and H Walther (Cambridge: Academic) vol 42 pp 95–170
[49] Safronova M S, Arora B and Clark C W 2006 Frequency-dependent polarizabilities of alkali-metal atoms from ultraviolet through infrared spectral regions *Phys. Rev.* A **73** 022505
[50] Meister M 2019 Novel concepts for ultra-cold quantum gases in microgravity: equal trap frequencies, atoms trapped by atoms, and the space atom laser *PhD Thesis* Universität Ulm
[51] Stellmer S, Grimm R and Schreck F 2013 Production of quantum-degenerate strontium gases *Phys. Rev.* A **87** 013611
[52] Hartwig J, Abend S, Schubert C, Schlippert D, Ahlers H, Posso-Trujillo K, Gaaloul N, Ertmer W and Rasel E M 2015 Testing the universality of free fall with rubidium and ytterbium in a very large baseline atom interferometer *New J. Phys.* **17** 035011
[53] Bordé C J 2001 Theoretical tools for atom optics and interferometry *C. R. Acad. Sci.- Series IV - Physics* **2** 509
[54] Roura A, Zeller W and Schleich W P 2014 Overcoming loss of contrast in atom interferometry due to gravity gradients *New J. Phys.* **16** 123012
[55] Roura A 2020 Gravitational redshift in quantum-clock interferometry *Phys. Rev.* X **10** 021014
[56] Hu H, Liu X-J and Modugno M 2003 Expansion of a quantum degenerate boson-fermion mixture *Phys. Rev.* A **67** 063614
[57] Schaff J-F, Capuzzi P, Labeyrie G and Vignolo P 2011 Shortcuts to adiabaticity for trapped ultracold gases *New J. Phys.* **13** 113017
[58] Onofrio R and Presilla C 2002 Reaching Fermi degeneracy in two-species optical dipole traps *Phys. Rev. Lett.* **89** 100401